ACS NANO

www.acsnano.org

ARTICLE

Tissue Imprinting on 2D Nanoflakes-Capped Silicon Nanowires for Lipidomic Mass Spectrometry Imaging and Cancer Diagnosis

Xingyue Liu,[‖] Zhao Chen,[‖] Tao Wang, Xinrong Jiang, Xuetong Qu, Wei Duan, Fengna Xi,* Zhengfu He,* and Jianmin Wu*

Cite This: *ACS Nano* 2022, 16, 6916−6928

Read Online

ACCESS | Metrics & More | Article Recommendations | Supporting Information

ABSTRACT: Spatially resolved tissue lipidomics is essential for accurate intraoperative and postoperative cancer diagnosis by revealing molecular information in the tumor microenvironment. Matrix-free laser desorption ionization mass spectrometry imaging (LDI-MSI) is an emerging attractive technology for label-free visualization of metabolites distributions in biological specimens. However, the development of LDI-MSI technology that could conveniently and authentically reveal molecular distribution on tissue samples is still a challenge. Herein, we present a tissue imprinting technology by retaining tissue lipids on 2D nanoflakes-capped silicon nanowires (SiNWs) for further mass spectrometry imaging and cancer diagnosis. The 2D nanoflakes were prepared by liquid exfoliation of molybdenum disulfide (MoS_2) with nitrogen-doped graphene quantum dots (NGQDs), which serve as both intercalation agent and dispersant. The obtained NGQD@MoS_2 nanoflakes were then decorated on the tip of vertical SiNWs, forming a hybrid NGQD@MoS_2/SiNWs nanostructure, which display excellent lipid extraction ability, enhanced LDI efficiency and molecule imaging capability. The peak number and total ion intensity of different lipids species on animal lung tissues obtained by tissue imprinting LDI-MSI on NGQD@MoS_2/SiNWs were ~4−5 times greater than those on SiNWs substrate. As a proof-of-concept demonstration, the NGQD@MoS_2/SiNWs nanostructure was further applied to visualize phospholipids on sliced non small cell lung cancer (NSCLC) tissue along with the adjacent normal tissue. On the basis of selected feature lipids and machine learning algorithm, a prediction model was constructed to discriminate NSCLC tissues from the adjacent normal tissues with an accuracy of 100% for the discovery cohort and 91.7% for the independent validation cohort.

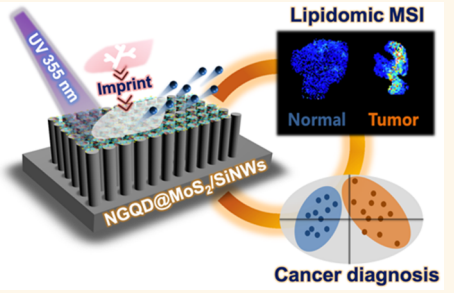

KEYWORDS: *lipidomics, mass spectrometry imaging, silicon nanowires, 2D nanoflakes, lung cancer*

INTRODUCTION

Precise diagnosis of cancer using metabonomics data has become a promising trend in recent years. More and more evidence have proven that metabolites, as the direct signatures of cell biochemical activity, can easily reflect cancer phenotype and progression.[1,2] Numerous studies have proven that lipid metabolites play a vital role in the development of cancer. Discovery and identification of key lipids that may drive cancer initiation and progression is crucial in clinical research.[3−5] Spatially resolved tissue lipidomics can reveal important molecular information for the assessment of cancer microenvironments during cancer progression, leading to the precise intraoperative and postoperative diagnosis. Compared with mature techniques for imaging of proteins in tissues (*e.g.*, immunohistochemistry-IHC), the spatially resolved detection technologies of lipid metabolites in various tissue samples are still under development.

As a powerful method with label-free properties and qualitative/quantitative capabilities, mass spectrometry imaging (MSI) can analyze the distribution of metabolites in tissues with high spatial resolution, providing molecular data related to cancer histopathology.[6] Matrix-assisted laser desorption ionization mass spectrometry imaging (MALDI-MSI) is considered as a very promising candidate method for biomarker discovery and disease diagnosis owing to its high-speed and robust performance.[7] It is usually necessary to homogeneously deposit matrix (usually an organic acid) on a

Received: March 16, 2022
Accepted: April 11, 2022
Published: April 13, 2022

https://doi.org/10.1021/acsnano.2c02616
ACS Nano 2022, 16, 6916−6928

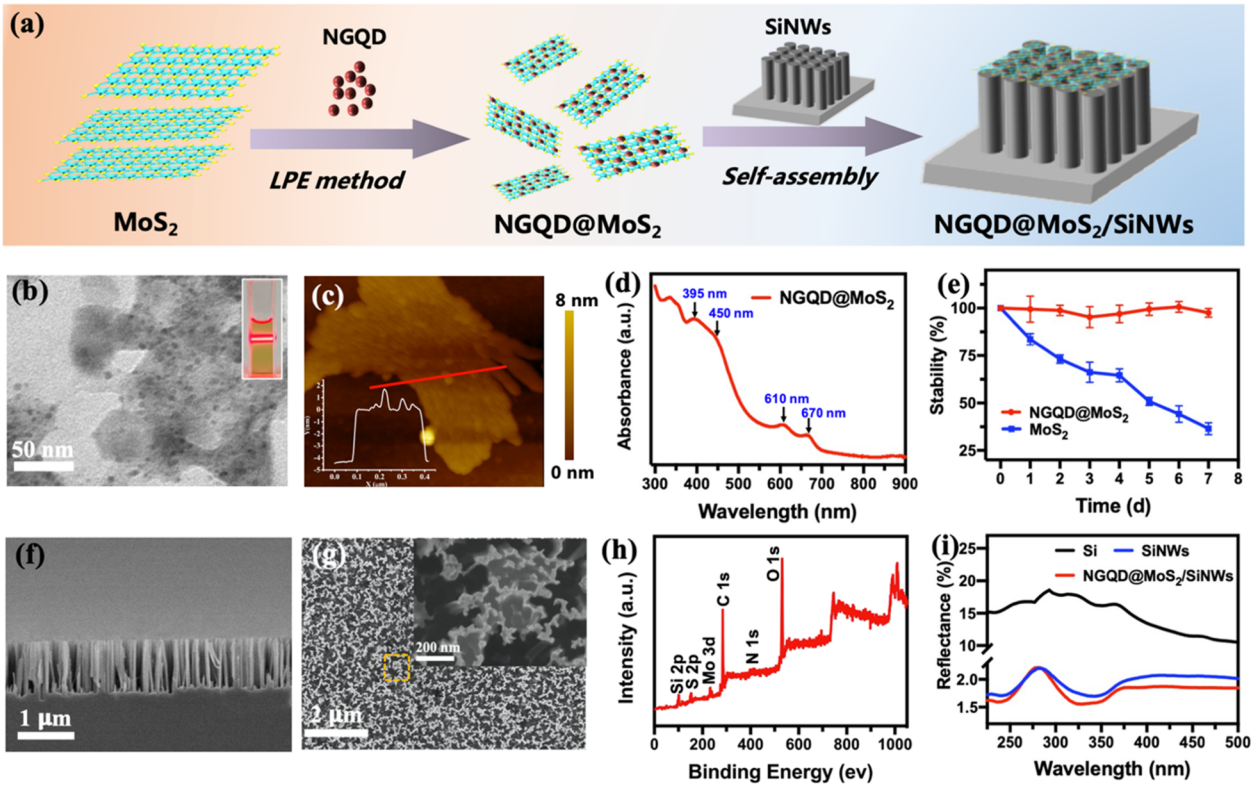

Figure 1. Construction of NGQD@MoS_2/SiNWs chip. (a) Schematic illustration of the fabrication of NGQD@MoS_2/SiNWs. (b) TEM image of NGQD@MoS_2 nanoflakes. Inset image is Tyndall effect of the aqueous dispersions of the obtained 2D nanoflakes. (c) AFM image and the corresponding height profiles (inset) for NGQD@MoS_2 nanoflakes. (d) UV−vis absorption spectrum of NGQD@MoS_2 nanoflakes. (e) Stability of NGQD@MoS_2 nanoflakes and MoS_2 nanoflakes. (f) Cross-sectional SEM image of the NGQD@MoS_2/SiNWs substrate. (g) Top overview SEM image of NGQD@MoS_2/SiNWs substrate and zoomed SEM image of the box region (inset). (h) Survey XPS spectrum of NGQD@MoS_2/SiNWs. (i) UV−vis DRS spectra of bare Si wafer, SiNWs, and NGQD@MoS_2/SiNWs.

tissue sample prior to the MALDI-MSI detection. However, the signal of metabolites could be serverely suppressed by the MS signals of matrix and analyte−matrix adducts in the low molecular range.[8,9] On the contrary, the "sweet-spots" caused by the nonuniform cocrystallization of the organic matrix will increase the signal variation, thereby reducing the accuracy for mapping metabolites distribution.[10] In addition, the process of matrix deposition is usually time-consuming and is often not suitable for most clinical practices. Therefore, fast and efficient laser desorption and ionization (LDI) methods for tissue lipidomic imaging are urgently needed.[11]

To address the above-mentioned problems, many matrix-free laser desorption ionization methods based on nanomaterials have been proposed.[9] Recent studies have proven that interaction between lasers and nanostructures enables a rapid and sharp increase of the surface temperature, promoting analytes desorption and ionization of the analyte.[12,13] Until now, various nanostructured carbon materials (*e.g.*, graphene,[14,15] multiwalled carbon nanotubes-MWCNT[16]), metal (*e.g.*, Au,[17−19] Pt[20]) materials, and silicon materials (porous silicon,[21] silicon nanopost arrays[22,23]) have been employed as substrates for laser desorption ionization mass spectrometry imaging (LDI-MSI) to visualize molecular distribution in tissue samples. Among them, vertical silicon nanowires (SiNWs) are ideal candidates for LDI analysis owing to high laser energy absorption and efficient energy and charge transfer abilities. Recently, our group found that an electric field could be concentrated at the tip of SiNWs, leading to significantly enhanced LDI ability.[24] At the same time, SiNWs can also be used as the sampling chips because molecules can be imprinted on the tips of SiNWs when SiNWs are in contact with tissue.[24] By analyzing the lipid molecules imprinted on the tip of SiNWs, a nondestructive MS method named as tip-contact sampling/ionization MS (TCSI-MS) has been developed to quickly acquire lipidomic information on liver tissue for hepatocarcinoma tumor identification.[25] The imprinting process can selectively transfer/adsorb analytes from a complex tissue surface onto the substrate, save pretreatment time, require lower laser energy, and improve anti-interference capability, compared with other LDI-MSI techniques. However, there still remains a challenge to use tissue imprinting technology as a imaging platform to precisely reveal the spatial distribution of lipids on tissues surface. To achieve the imaging capability of tissue imprinting technology, modulation of the nanostructure surface is highly important, since the surface structure will not only affect the imprinting efficiency but also influence the performance of energy transfer and charge transfer on the interface upon the irradiation of a laser on the nanostructure. Meanwhile, the regulation of the nanostructure may effectively avoid the problem of "sweet-spots" that also exist in nanostructure-assisted LDI. Eliminating the sweet-spots problem will have a great influence on the precise mapping of molecular distribution. On the basis of our previous work of TCSI-MS, further efforts to modify SiNWs for improving tissue imprinting efficiency and lipid imaging ability are highly desirable.

So far, several nanomaterials such as Au nanoparticle,[26] Ag nanoparticle,[27] and graphene[25] have been explored to modify a

https://doi.org/10.1021/acsnano.2c02616
ACS Nano 2022, 16, 6916−6928

Si-based substrate for improving LDI efficiency. However, metal nanoparticles deposition might still cause sweet-spots because of their heterogeneity in solid state.[28,29] Carbon-based nanomaterials usually suffer from intense carbon cluster peaks in the low-mass region when irradiated with high laser energy density.[30] As a low-cost and photosensitive material, 2D MoS_2 nanoflakes have great potential in promoting LDI efficiency, taking advantage of high light absorption and energy enrichment capacity in the UV−visible range.[31,32] In addition, high affinity toward phospholipids makes MoS_2 suitable for imprinting tissue lipids before LDI-MSI analysis.[33] However, there still exists an obstacle to obtain stable few-layers MoS_2 nanoflakes in solution, and reaggregation is hard to avoid. In addition, the rapid recombination of photogenerated electron−hole pairs and the limited active edge sites in MoS_2 also hinder the performance of LDI.[34]

In the present work, we used bottom-up grown nitrogen-doped graphene quantum dots (NGQDs) as both the intercalation agent and dispersant to assist liquid exfoliation of MoS_2. Using this approach, stable and well-dispersed 2D nanoflakes with NGQD@MoS_2 heterojunctions were obtained. The 2D nanoflakes were then loaded on the tip of vertical SiNWs *via* a self-assembly process to obtain NGQD@MoS_2/SiNWs substrate for tissue imprinting LDI-MSI. The LDI efficiency of lipid molecules with different polarities was significantly improved on the NGQD@MoS_2/SiNWs substrate owing to its higher photothermal conversion and photo-induced charge transfer efficiency of NGQD@MoS_2/SiNWs. Furthermore, the sweet-spot effect could be elinimated because the capping of 2D nanoflake on SiNWs could delocalize thermal energy and homogenize the LDI efficiency on the whole chip surface. Being free of the sweet-spot is highly important in the spatial-resolved relative quantitation of biomolecules on tissue. With this platform, the abundance and distribution of phospholipids on sliced NSCLC tissue and the adjacent normal tissue were authentically revealed by TCSI-MS imaging (TCSI-MSI). On the basis of feature lipids selected from both groups, a prediction model was constructed by a machine learning algorithm, which can discriminate NSCLC tissues from the adjacent normal tissues with an accuracy of 100% for the discovery cohort and 91.7% for the independent validation cohort. We believe the tissue imprinting technology using NGQD@MoS_2/SiNWs substrate might serve as a powerful TCSI-MSI platform for wide clinical appilication.

RESULTS AND DISCUSSION

Fabrication and Characterization of NGQD@MoS_2/SiNWs Substrate. The fabrication of NGQD@MoS_2/SiNWs was illustrated in Figure 1a. First, the SiNWs array was prepared by one-step metal-assisted chemical etching (MACE) of a silicon wafer[35] (Figure S1a). The as-prepared SiNWs display a well-aligned and vertical array structure with an average diameter and length of ∼50 nm and 1 μm, respectively (Figure S1b,c). Our previous work demonstrated that the obtained SiNWs array displays good laser absorption capability in the near-ultraviolet region for LDI detection,[24] and most of the laser energy would be absorbed and accumulated at the tip section. To improve the imaging performance of the substrate, the 2D MoS_2 nanoflake exfloited with zero-dimensional (0D) NGQD was chosen as a "cap" to modifiy the tip of SiNWs. Herein, a NGQD-asisted liquid-phase exfoliation (LPE) method was used to obtain few-layered 2D MoS_2 nanoflakes, because NGQD could intercalate into and interact with 2D materials more effectively.[36] The bandgap energy of 2D MoS_2 drastically reduced with the decrease of layer number. It has been reported that the few-layered 2D MoS_2 as a narrow gap semiconductor exhibits good light−matter interactions and high carrier mobility.[37,38] If the few-layered 2D MoS_2 is loaded on SiNWs, the hybrid nanomaterials will enhance laser absorption and charge separation ability owing to the formation of heterojunctions.[39,40] On the contrary, the attached NGQD, as a effective collector for charge carrier, will further reduce the recombination of photogenerated electrons and holes.[34,41] The increased charge lifetime and high charge mobility of NGQD@MoS_2 will contribute to promoting charge transfer between analytes and the nanomaterials in the LDI process. Therefore, the decoration of NGQD@MoS_2 nanoflakes on SiNWs array should be a good way to improve the LDI efficiency of SiNWs.

A hydrothermal method was used to synthesize NGQD according to previous work.[42] The transmission electron microscopy (TEM) and atomic force microscopy (AFM) images reveal that the produced NGQDs are uniformly sized with an average diameter of ∼2 nm and thickness of ∼1.4 nm (Figure S2). Afterward, MoS_2 nanoflakes were exfoliated by NGQDs acting as both an intercalation agent and dispersant. TEM images reveal that the MoS_2 nanoflakes are successfully decorated with NGQDs (Figure 1b) compared with morphologies of the MoS_2 in the absence of NGQD (Figure S3). It should be noted that the contrast of the NGQD@MoS_2 in the TEM image is lighter than that of MoS_2, attributing to the thinner layer of NGQD@MoS_2 with the assistance of NGQD exfoliation. The Tyndall phenomenon (inset picture in Figure 1b) apparently shows the good water dispersibility of the NGQD@MoS_2 nanoflakes. The AFM image further indicates that the diameter and thickness of NGQD@MoS_2 nanoflakes are approximately 200−300 and 4.0 nm, respectively (Figure 1c). The height profiles of AFM reveal that NGQDs with a size of 1−3 nm are randomly distributed on MoS_2 nanoflakes. Dynamic light scattering (DLS) also indicates that the average hydrodynamic radius of the NGQD@MoS_2 nanoflakes is 200 ± 50 nm (Figure S4a), which is consistent with the AFM result. UV−vis absorption spectra of NGQD@MoS_2 nanoflakes dispersed in water/ethanol solution further confirm the successful exfoliation of MoS_2. The characteristic absorption peaks at 395, 450, 610, and 670 nm suggest the existence of a layered 2H-MoS_2 structure (Figure 1d). The excitonic peaks at 610 and 670 nm arise from the K point of the Brillouin zone, while the other two peaks are attributed to the direct transition from the deep valence band to the conduction band.[36] The stability of MoS_2 and NGQD@MoS_2 aqueous solution was further investigated by UV−vis absorption spectroscopy (Figure 1e). Without NGQD-assisted LPE, the MoS_2 nanoflakes aggregate and precipitate quickly in 7 days (Figure S4b), leading to the gradually decrease of UV−vis absorption. In contrast, the UV absorption spectra of the NGQD@MoS_2 aqueous solution were quite stable after 7 days (Figure S4c), confirming the significance role of NGQD intercalation.

Afterward, the obtained 2D NGQD@MoS_2 nanoflakes were used to modify SiNWs substrate for enhancing the performance of tip contact sampling and LDI efficiency. The vertical SiNWs were premodified with (3-aminopropyl) triethoxysilane (APTES) to obtain a positively charged surface and impart affinity for NGQD@MoS_2 nanoflakes, which has a negative ζ

https://doi.org/10.1021/acsnano.2c02616
ACS Nano 2022, 16, 6916−6928

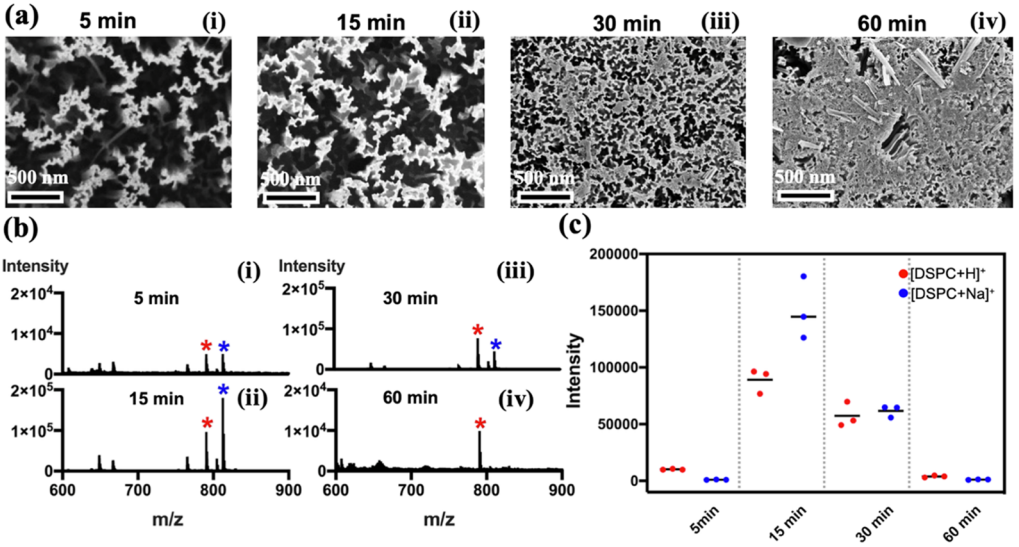

Figure 2. Optimization of NGQD@MoS_2/SiNWs chip for LDI-MS. (a) Top-view SEM images of NGQD@MoS_2/SiNWs chip with different self-assembly times of (i) 5 min, (ii) 15 min, (iii) 30 min, and (iv) 60 min. (b) Representative mass spectra of 0.1 mg mL^{-1} DSPC on the NGQD@MoS_2/SiNWs chip with different self-assembly times of (i) 5 min, (ii) 15 min, (iii) 30 min, and (iv) 60 min. (c) Mean intensities with hydrogen and sodium adduct peaks (red for $[DSPC + H]^+$ and blue for $[DSPC + Na]^+$.

potential of −36.3 mV (Figure S5). The ζ potential indicates that the NGQD@MoS_2 nanoflake is negatively charged, which also contributes to the stabilization of NGQD@MoS_2 in suspension. Owing to the electrostatic interaction force, the as-prepared NGQD@MoS_2 nanoflakes could be spontaneously decorated on the top of APTES-modified SiNWs *via* a self-assembly process. After a suitable time of self-assembly, NGQD@MoS_2 nanoflakes uniformly distributed and capped on the tip of vertical SiNWs (Figure 1f,g), forming the hybrid structure of NGQD@MoS_2/SiNWs. The composition and chemical state of the NGQD@MoS_2/SiNWs substrate were explored by X-ray photoelectron spectroscopy (XPS), in which O, N, C, Mo, S, and Si elements were observed (Figure 1h). The deconvoluted XPS spectrum exhibits two characteristic peaks at 228.6 and 232.0 eV, which correspond to the Mo $3d_{5/2}$ and Mo $3d_{3/2}$ orbitals, respectively (Figure S6a), suggesting a Mo(IV) valence state in MoS_2.[43] As for the spectrum of S 2p (Figure S6b), the binding energies located at 161.5 and 163.5 eV could be ascribed to S $2p_{3/2}$ and $2p_{1/2}$, respectively, indicating Mo−S bonding in MoS_2.[44] The XPS spectra of N 1s verify the successful doping of N in the hybrid nanocomposites. As shown in Figure S6c, it could be deduced into four peaks centered at about 399.2 and 402.3 eV, which are assigned to pyrrolic N and N−H, respectively.[42]

The UV−vis diffuse reflectance spectroscopy (DRS) spectra (Figure 1i) shows that vertical SiNWs absorb most of UV light with a reflectance of ∼2%, while bare Si wafer reflects ∼15% of UV light. It should be noted that high optical absorption at 355 nm (the wavelength of the laser used by MALDI) is considered to be a crucial factor in the LDI process. After capping vertical SiNWs with NGQD@MoS_2 2D nanoflakes, the UV reflectance further decreased. The low reflectance is benefical for energy conversion in laser desorption and ionization processes.

Optimization of NGQD@MoS_2/SiNWs for LDI-MS. As discussed above, the decoration of NGQD@MoS_2 nanoflakes is expected to enhance the LDI performance of SiNWs owing to higher photothermal conversion and enhanced photo-induced charge transfer efficiency. However, the thickness of the NGQD@MoS_2 nanoflake layer on vertical SiNWs needs to be optimized since the amount and thickness of 2D nanomaterials is tightly associated with their LDI efficiency. By controlling the time of self-assembly from 5 to 60 min, the thickness of NGQD@MoS_2 nanoflake capped on vertical SiNWs gradually increases (Figure 2a). NGQD@MoS_2 nanoflakes are not observed when the time is 5 min. After increasing the self-assembly time to 15 min, a uniform thin nanoflake layer is formed at the top of vertical SiNWs, with a clear vision of the nanowire tip. When the self-assembly time reaches 60 min, the vertical SiNWs structure is fully covered by a thick layer of NGQD@MoS_2 nanoflakes, resulting in the disappearance of the tip of SiNWs. Our previous work indicated that the tip structure is crucial to improve the LDI efficiency since the tip of vertical SiNWs could effectively concentrate and confine the laser energy.[24] The LDI performance of the NGQD@MoS_2/SiNWs substrates with different times for self-assembly of NGQD@MoS_2 was evaluated by 1,2-distearoyl-*sn*-glycero-3-phosphocholine (DSPC) lipids on the LDI-MS platform. Compared with vertical SiNWs without capping of NGQD@MoS_2, the LDI efficiency of NGQD@MoS_2/SiNWs generally increases except for the sample at 5 min (Figure 2b,c), suggesting that the capping effect is insignificant with a short time of self-assembly process. With a self-assembly time of 15 min, the best LDI efficiency and highest S/N ratio for the standard analyte detection are achieved. If the self-assembly time reaches 30 min, the LDI efficiency significantly reduces due to the agglomeration of NGQD@MoS_2 on the SiNWs surface and tends to diminish the efficiency of photoinduced electron transfer at the NGQD@MoS_2/SiNWs interface. In addition, the thick capping layer also reduced the tip structure, leading to the decrease of laser energy concentration. Thus, 15 min was selected as the optimized time to construct the NGQD@MoS_2/SiNWs substrate for further investigations.

To further validate the performance of LDI efficiency and advantage of the NGQD@MoS_2/SiNWs, a series of substrates including MoS_2/SiNWs, NGQD/SiNWs, and SiNWs were fabricated and their LDI efficiencies were compared. Three representative standard lipids including 1,2-dipalmitol-*sn*-

https://doi.org/10.1021/acsnano.2c02616
ACS Nano 2022, 16, 6916−6928

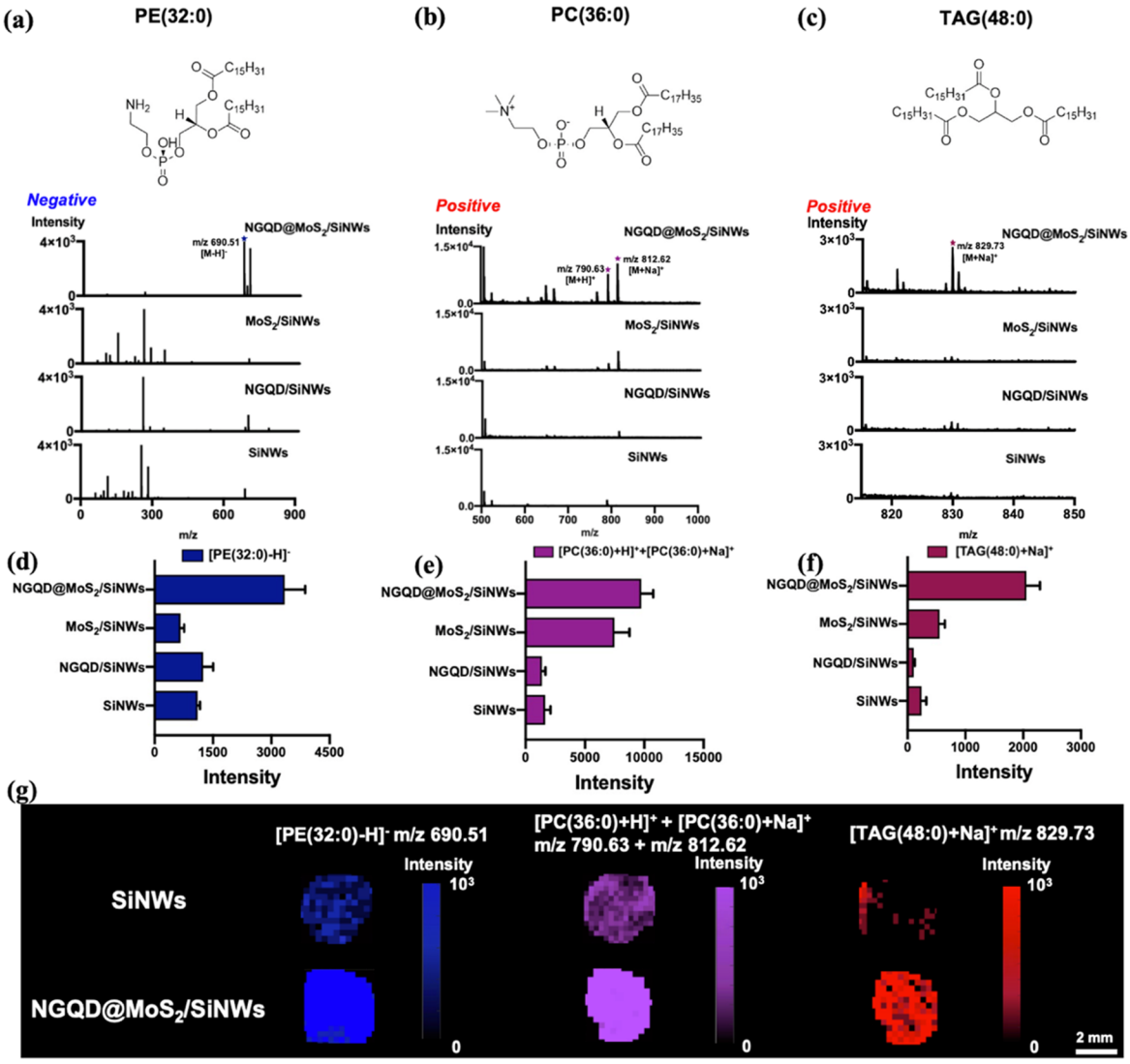

Figure 3. (a–c) Molecular structures of PE(32:0), PC(36:0), and TAG(48:0), respectively, and representative spectra of 1 mg mL^{-1} PE(32:0), 1 mg mL^{-1} PC(36:0), and 1 mg mL^{-1} TAG(48:0) on different chips. Mean intensities of (d) $[M - H]^-$ signals of 1 mg mL^{-1} PE(32:0), (e) $[M + H]^+$ and $[M + Na]^+$ signals of 1 mg mL^{-1} PC(36:0), and (f) $[M + Na]+$ signals of 1 mg mL^{-1} TAG(48:0) obtained using different chips; the error bars were calculated as SD of three measurements. (g) Mass images of standard droplets on SiNWs and NGQD@ MoS_2/SiNWs.

glycero-3-phosphoethanolamine (PE(32:0)), 1,2-distearoyl-*sn*-glycero-3-phosphocholine (PC(36:0)), and 1,1′,1″-(1,2,3-propanetriyl) ester (TAG(48:0)) with different electric polarities were applied as model molecules for measuring the LDI efficiency. PE(32:0) was detected as $[M - H]^-$ in negative ion mode (Figure 3a), while PC(36:0) was detected as $[M + H]^+$ and $[M + Na]^+$ adducts in positive mode (Figure 3b). Neutral lipid TAG(48:0) was detected as $[M + Na]^+$ adducts in positive mode (Figure 3c). The averaged intensity of these ions by three repeated scans on different substrates were compared (Figure 3d–f). The results indicate that NGQD@MoS_2/SiNWs achieves the best LDI efficiency for the standard lipids with different ion polarities.

Another important aspect as an alternative LDI-MSI substrate is to obtain a uniform signal on the surface without sweet-spots. To investigate this effect, 2 μL of each standard solution was spotted on NGQD@MoS_2/SiNWs or SiNWs substrate, respectively. The molecular mass intensity images of deposited region were acquired with a 150 μm laser width. As shown in Figure 3g, the images obtained on NGQD@MoS_2/SiNWs show a more homogeneous signal distribution than that on SiNWs. The relative standard deviation (RSD) of lipid signal intensity obtained from every pixel was calculated to evaluate the variation of signal intensity distributed on the substrate surface (Figure S7). The RSD of NGQD@MoS_2/SiNWs substrate is 15%~48% for the three lipid molecules, while for SiNWs substrate, the RSD value is between 65% and 84%. Thus, the NGQD@MoS_2/SiNWs substrate has great advantage of avoiding sweet-spots. The formation of a homogeneous sample spot with relatively uniform mass peak intensities might be ascribed to the delocalization of laser energy after bridging the tip of SiNWs by a thin layer of 2D NGQD@MoS_2 nanoflakes. The specific properties of the NGQD@MoS_2/SiNWs make it an ideal MSI substrate for quantitative analysis and authentic visualization of lipids distribution for tissue sample.

Synergistic Effect and Mechanism of NGQD@MoS_2/SiNWs Substrate. To verify the synergistic effect of NGQD@

https://doi.org/10.1021/acsnano.2c02616
ACS Nano 2022, 16, 6916–6928

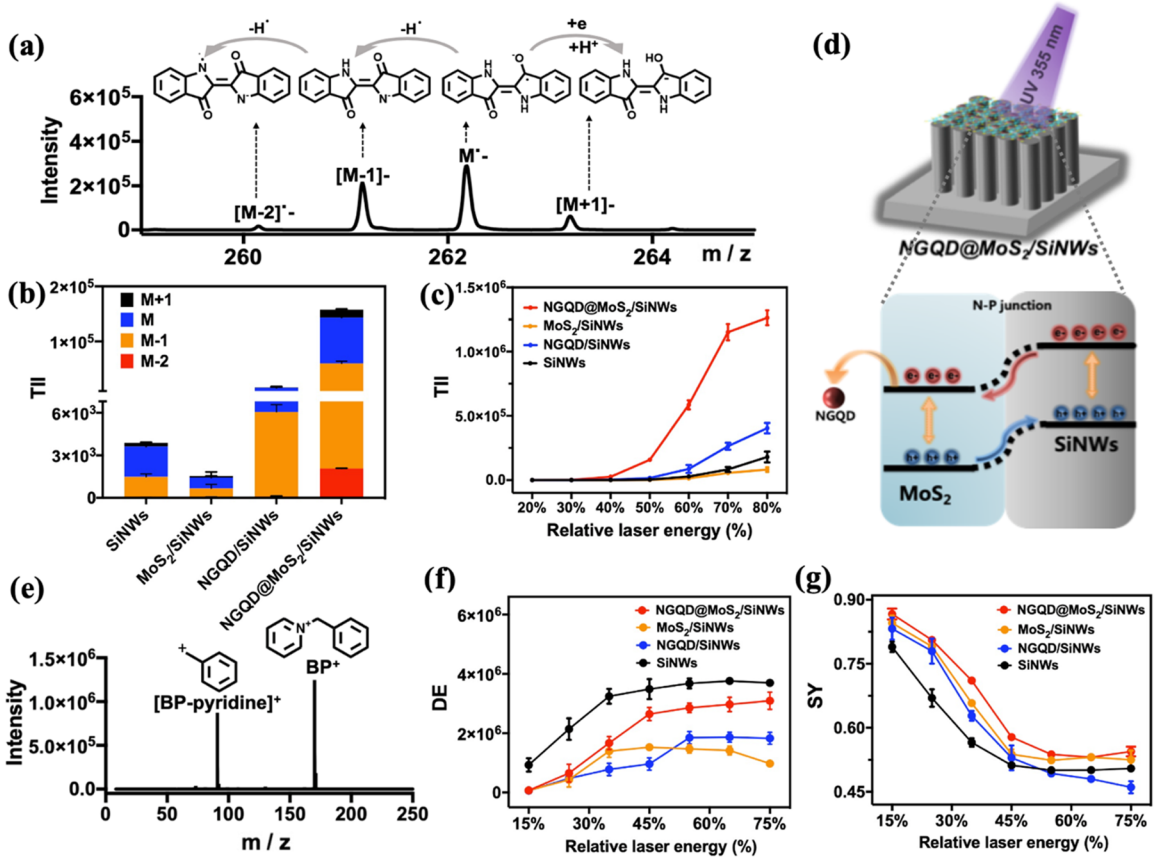

Figure 4. (a) Chemical structure and mass spectrum of indigo molecule. (b) Total ion intensity (TII) and ion distribution map of indigo under 50% laser energy. (c) TII curves of indigo on four different chips under different relative laser energies. (d) Schematic illustrations of the charge transfer in the laser desorption and ionization process. (e) Chemical structure and mass spectrum of BP molecule. (f and g) Desorption efficiency (DE) and survival yield value (SY) of the BP molecule on four different chips with different laser energies.

MoS_2/SiNWs composites in LDI-MS, indigo was selected as a model molecule to investigate photoinduced electron and proton transfer process on different substrates.[24,45] In negative ion mode, charge transfer plays a major role in LDI process. Indigo has two sites that can accept electrons and lose protons, producing a series of negative ions including $[M]^{-\cdot}$, $[M + H]^-$, $[M - H]^-$, and $[M - 2H]^{-\cdot}$ at m/z 262.077, 263.083, 261.068, and 260.056, respectively (Figure 4a). The total ion intensity (TII) of these ions obtained on the NGQD@MoS_2 /SiNWs substrate is 40, 9, and 93 times higher than those obtained on SiNWs, NGQD/SiNWs, and MoS_2/SiNWs, respectively (Figure 4b). In contrast, the intensity of the indigo peak generated on MoS_2, NGQD, or NGQD@MoS_2 without SiNWs substrate is far less than that generated on the nanomaterials with SiNW (Figures S8 and S9). The results confirm the critical role of SiNWs and the synergestic effect between NGQD@MoS_2 and SiNWs in the LDI process. We also find that NGQD@MoS_2/SiNWs exhibits a lowest energy threshold and greatest signal enhancement, as shown in Figure 4c. At the same time, a slight reduction in intensities can be observed on MoS_2/SiNWs compared to those with pure SiNWs. The formation of a n−p heterojunction between MoS_2 and SiNWs may have increased the electron transfer rate. However, due to the high rate of electron−hole pair recombination on thick MoS_2 itself, the lifetime of photo-induced electron will reduce compared to that of pure SiNWs. NGQD have been found to be beneficial to boost the charge transfer and restrain the recombination of photoinduced electron−hole pairs.[46] In addition, NGQDs/MoS_2 acts an efficient photoelectrochemical (PEC) biosensor for enhanced charge−carrier lifetime.[34] In the present work, an improvement of TII on NGQD/SiNWs is observed compared to that on SiNWs, confirming the role of NGQD in charge transfer. By decoration of NGQD on MoS_2 nanoflakes, the n−p heterojunction can further facilitate the electron transfer rate and inhibit the recombination of electron−hole pairs, resulting in a significant improvement of photoinduced electron transfer on the NGQD@MoS_2/SiNWs interface. This mechanism for depicting the synergistic effect is illustrated in Figure 4d.

Investigating the relationship of LDI efficiency and internal energy transfer could provide useful information on mining the factors to govern the desorption/ionization process. Referencing previous works,[47] benzylpyridinium (BP) salts were adopted as the "thermometer chemical" to investigate the effects of various substrates on the ion desorption efficiency (DE = $I[BP]^+ + I[BP\text{-}pyridine]^+$) and to probe the extent of internal energy transfer in the desorption process on the basis of the survival yield (SY = $I(BP^+)/[I(BP^+) + I[BP\text{-}pyridine]^+]$), as showin Figure 4e. In general, the higher DE and SY values are associated with more effective desorption and less fragmentation of analyte, thereby increasing the sensitivity in MS detection. The DE and SY values obtained on four different substrates under different relative laser energies (from 15% to 75%) were measured with a BP probe (Figure 4f,g). The results indicate that the SY of BP on SiNWs is 54%, whereas it increases to 65% on MoS_2/SiNWs and further

https://doi.org/10.1021/acsnano.2c02616
ACS Nano 2022, 16, 6916−6928

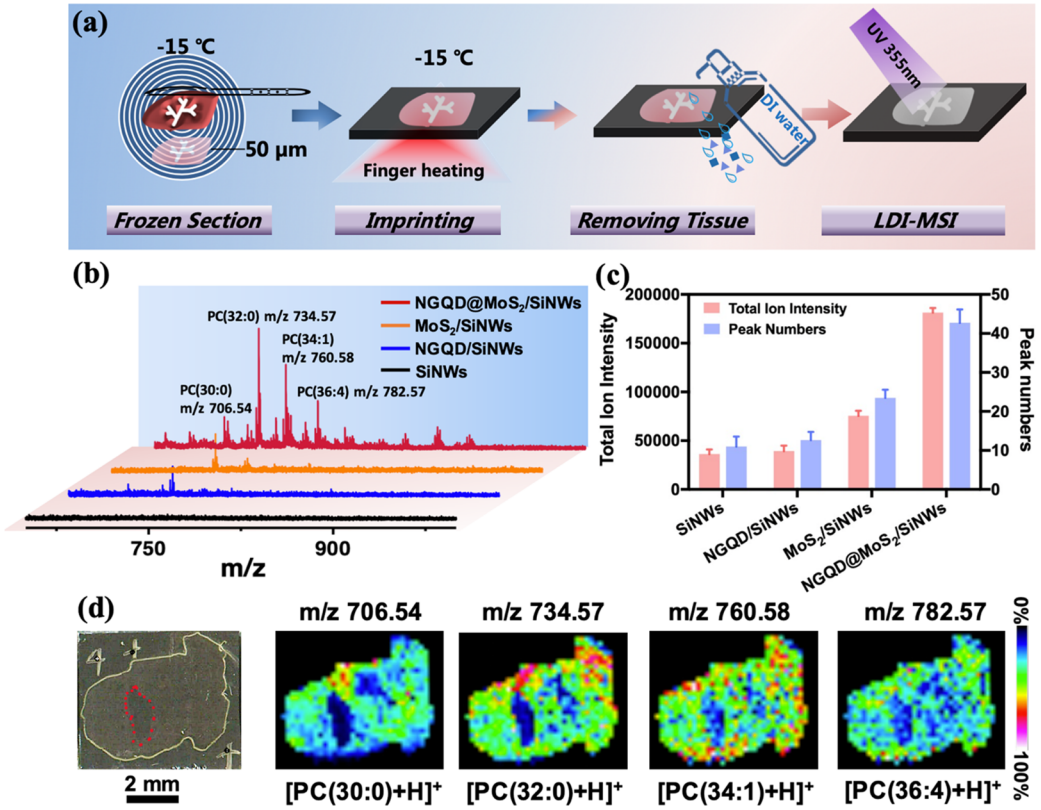

Figure 5. (a) Schematic workflow of LDI-MSI of lipid molecules imprinted from tissue. (b) Overall average spectra of lung tissues detected in four different substrates. (c) Total ion intensity of peaks ($S/N > 5$) and peak numbers ($S/N > 5$) detected from four different substrates within m/z 700−900. (d) Digital image of the substrate imprinted by mouse lung tissue and typical ion mass spectrometry imaging of mouse lung tissue.

increases to 71% on NGQD@MoS_2/SiNWs under a relative laser energy of 35%. This could attribute to the synergistic effect of thermal conductivity between MoS_2 and SiNWs and the sp^2 domains as a thermal sink during the rapid thermalization of laser-excited electrons,[48] leading to the decrease of internal energy transfer and increase of SY values. In contrast, the DE value on the NGQD@MoS_2/SiNWs is lower than that on the SiNWs, due to the dissipation of absorbed laser energy. The significant reduction in the desorption efficiency of MoS_2/SiNWs and NGQD/SiNWs might be ascribed to the poor photothermal performance. These results indicate that the desorption efficiency and the degree of fragmentation are dependent on the materials of the substrate. NGQD@MoS_2/SiNWs show a great advantage of reducing fragments, despite the undesired but suitable decreasing of desorption efficiency, which could greatly enhance the mass ion signal intensity to detect lipids with longer fatty acid chains.

TCSI-MSI of Lipid Molecules Imprinted from Mouse Lung Tissues. After successful construction of the TCSI-MSI substrate, another main objective of this work is to verify the capability of the NGQD@MoS_2/SiNWs substrate to imprint tissues lipids for further LDI-MS imaging. As a proof of concept, a mouse lung tissue was used to analyze lipid molecules transferred from lung tissue. The imprinting technique for MSI has several advantages including time-saving, low laser energy requirement, and high anti-interference capability.[49] To demonstrate the performance of the NGQD@MoS_2/SiNWs substrate for tissue-imprinted TCSI-MSI, sliced mouse lung sections with 50 μm thickness were separately imprinted on to NGQD@MoS_2/SiNWs, MoS_2/SiNWs, NGQD/SiNWs, and SiNWs substrates using an optimized workflow (Figure 5a) and then analyzed in positive ion mode, respectively. The overall average mass spectra are shown in Figure 5b. The peak numbers and total ion intensity obtained on the NGQD@MoS_2/SiNWs substrate are significantly higher than the other three types of substrate (Figure 5c). The peak numbers (MS signals with a signal-to-ratio larger than 5 between m/z 700−1000) obtained on NGQD@MoS_2/SiNWs is ∼4 times greater than those on SiNWs. The total ion intensity of lipid signals on NGQD@MoS_2/SiNWs is ∼5 times greater than that on SiNWs. Among them, more than 20 lipid species were putatively annotated, mainly in H^+ adduct forms. Most of these ions have already been reported.[50] The results could be contributed to the stronger LDI efficiency and high affinity of the NGQD@MoS_2/SiNWs substrate for tissue lipids.[33]

The spatial resolved distribution of sliced mice lung sections was further evaluated by the tissue imprinting TCSI-MSI in positive ion mode with a laser width of 150 μm (Figure 5d). The ion images clearly display cavities (red dashed circle) in lung tissues, which can match with the real morphology of tissue sample, indicating that the workflow of sample preparation by the NGQD@MoS_2/SiNWs substrate has good control of the lateral diffusion of analytes. It is worth noting that phosphatidylcholines were only detected as the protonated molecules. In MALDI or most LDI-MSI, they were usually detected in various forms such as $[PC + H]^+$, $[PC + Na]^+$, and $[PC + K]^+$ ions, which may cause isobaric interferences.[51] The washing step in the protocol removes

https://doi.org/10.1021/acsnano.2c02616
ACS Nano 2022, 16, 6916−6928

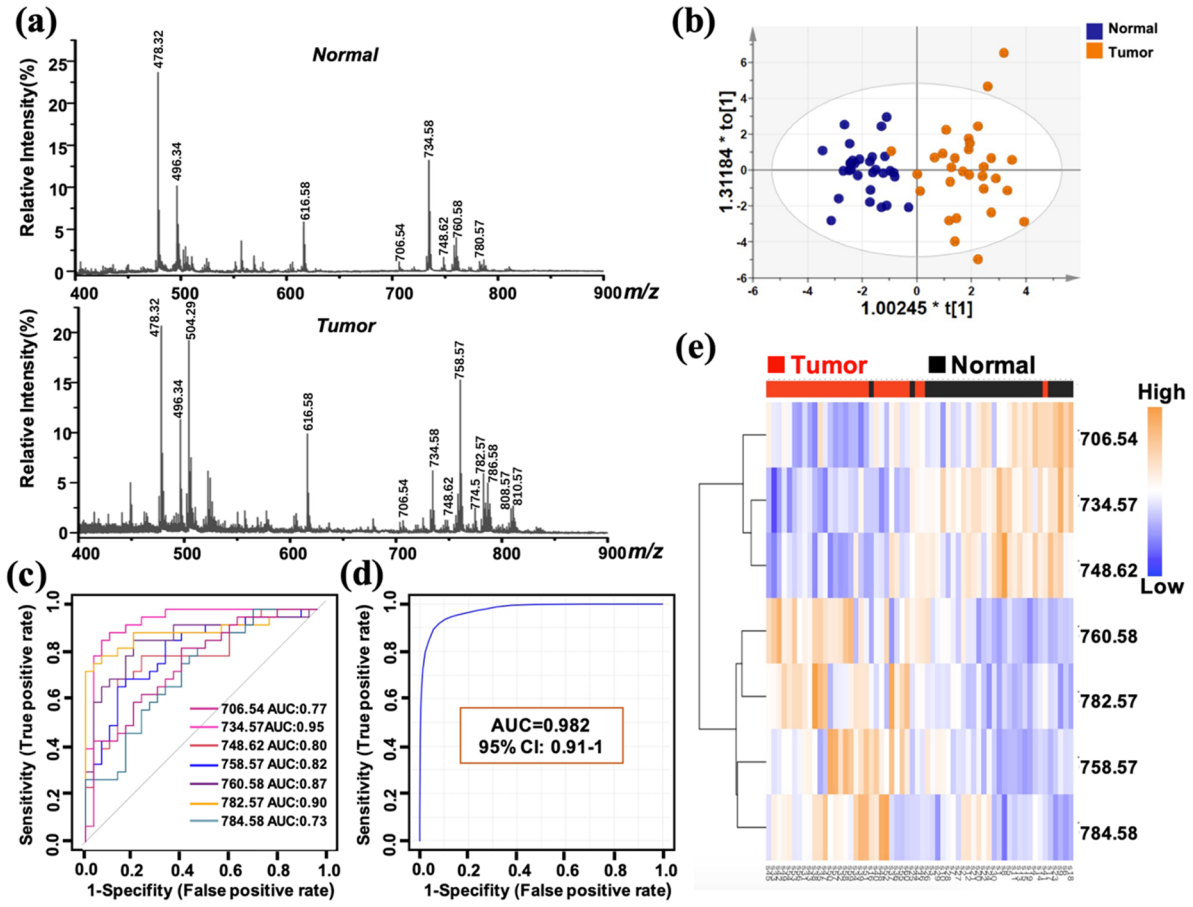

Figure 6. Precise discrimination of NSCLC tissues. (a) Overall average mass spectra of normal and tumorous tissues. (b) OPLS-DA score plots of metabolites from tumorous tissues (orange dots) and the adjacent normal tissues (blue dots). (c) Receiver operator characteristic (ROC) curves differentiating tumorous tissues from normal tissues of individual biomarker and the corresponding AUC values. (d) ROC curve obtained by the panel of combined biomarkers with AUC of 0.982 across a 10-fold cross validation. (e) Hierarchical clustering analysis (HCA) of normal and tumorous tissues.

salts and therefore eliminates these cationized species that overlap with other isobaric species, hence simplifying spectra interpretation and showing beneficial imaging of lipids imprinted from tissues. Compared to another LDI-MSI method for lipid using traditional crystalline matrixes (2,5-dihydroxybenzoic acid (DHB),[52] *etc.*) and nanoparticles (Au,[17] Ag,[53] *etc.*), which need a complex matrix spray and deposition process on an additional supporting substrate such as indium tin oxide (ITO) glass and stainless steel plates, the 2D nanoflake-capped SiNWs composite structure can be used as both a high-performance marix-free LDI substrate and effective sampling chip, taking only ~10 min for sample preparation before MS imaging. In addition, the convenient and non-destructive tissue imprinting procedure requires low laser energy and has high anti-interference capability, which can be better integrated and coordinated with clinical research toward precision medicine.

Lipid Profiling and Imaging of Non Small Cell Lung Cancer (NSCLC) Tissues. Lung cancer is one of the most widely spread cancers worldwide, accounting for the highest rate of cancer-related mortality.[54] Clinical lipidomics has demonstrated that the expression of lipid in lung tissue is highly correlated with metabolic diseases and subtypes of lung cancer.[4] To prove the applicability of the NGQD@MoS_2/SiNWs as the tissue imprinting TCSI-MSI substrate for lung cancer biomarker discovery, 30 pairs of clinical NSCLC tissues and corresponding adjacent normal tissues were collected. All of the sample demographic information has been summarized in Table S1. The mass spectra of each sample were obtained by complete detection mode in the imprinted region on substrates and averaged by three scans. Mass ion images were obtained with 150 μm spatial resolution. As shown in Figure 6a, significant differences are observed in the mass spectra of tissue lipids between the tumor tissue and adjacent normal tissue. Most of acquired peaks at the range m/z 700−1000 are identified as phosphatidylcholine (PC), a major lipid class that occurred in the microenvironment of lung tissue.[55] On the basis of orthogonal partial least-squares discriminant analysis (OPLS-DA), a clear group separation between NSCLC tissues and the adjacent normal tissues was observed (Figure 6b). We further performed S-plot and t test to discover reliable lipid biomarkers. As a result, seven lipids with a variable importance in projection (VIP) score >1 and a P value <0.0001 were selected as the feature panel (Table S2), and their structure was indentified (Table S3). Hierarchical clustering analysis based on a feature lipid panel also confirmed the successful differentiation of tumor tissue from the adjacent tissue (Figure 6c). To validate the reliability of these putative lipid biomarkers, the receiver operating characteristic (ROC) analysis was performed. The area under the curve (AUC) values were calculated for all potential biomarkers (Figure 6d), within the range 0.73−0.95. Then, all biomarkers were

https://doi.org/10.1021/acsnano.2c02616
ACS Nano 2022, 16, 6916−6928

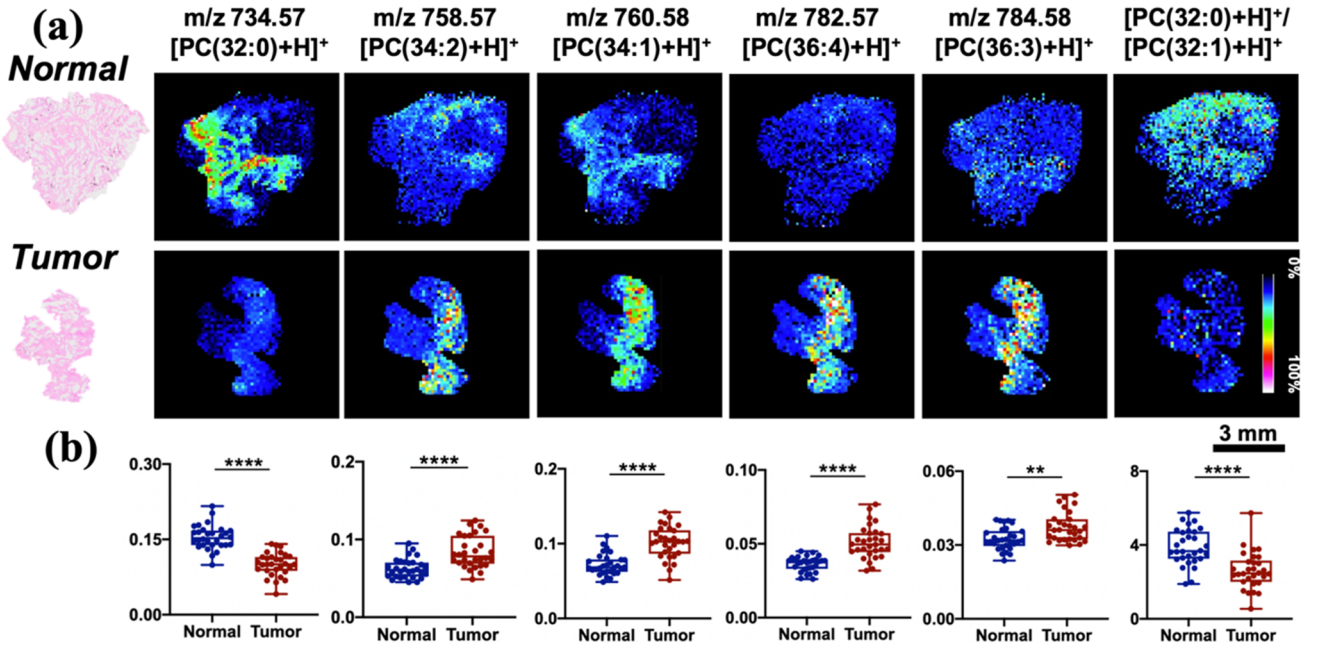

Figure 7. Distribution of representative biomarkers in adjacent normal and tumorous tissues from NSCLC tissue. (a) Distribution of representative potential biomarkers across tissue sections from NSCLC tissue: Row 1, images of corresponding H&E-stained section and ion images from adjacent normal tissue sections; Row 2, images of corresponding H&E-stained sections and ion images from tumorous tissue sections. (b) Statistical box plots showing the ion intensity of the tumorous and adjacent normal tissue sections with the degree of differentiation. (, $p < 0.01$; ****, $p < 0.0001$) .**

combined by binary logistic regression for ROC analysis to evaluate discrimination performance. The combined lipid panel shows the best discrimination between tumor and normal tissue with an AUC of 0.982 (Figure 6e). Furthermore, to evaluate whether these features can be used for precisely predict NSCLC tumor tissue, an artificial neural network (ANN) was conducted with the workflow shown in Figure S10. Using 48 clinical NSCLC tissue and the adjacent normal tissue samples as modeling construction, a sensitivity of 100% and a specificity of 100% with an overall accuracy of 100% can be accomplished in the training, validation and test subsets using the selected seven features as a biomarker panel (Figure S11a). In addition, another 12 clinical NSCLC tissues and the adjacent normal tissue samples were analyzed and predicted as a test group using this ANN model. In this test, a 91.7% prediction accuracy can be obtained (Figure S11b), verifying that the selected lipid panel can accurately diagnosis NSCLC tissues.

After the discovery of a feature lipid panel, their spatial-resolved distribution on the sliced lung tissure was visualized with TCSI-MSI (Figure 7a). The MS peaks at m/z 758.57 (PC(34:2)), 760.58 (PC(34:1)), 782.57 (PC(36:4)), and 784.58 (PC(36:3)) reveal a upregulation trend in tumor tissue while m/z 734.57 (PC(32:0)) reveals a downregulation trend (Figure 7b). In previous reported literatures,[56,57] similar trends of PC 34:1 and PC 32:0 have also been found for distinguishing lung cancer tissues. Meanwhile, it is worth noting that the ratio of saturated lipids to monounsaturated lipids (MUPC) (PC32:0 (m/z 734.57)/PC32:1(m/z 732.57)) shows a significant downregulation trend in tumor tissues, indicating that NSCLC tissues have a higher expression of MUPC than normal tissues as reported previously.[58] The results could be caused by the action of stearoyl-CoA desaturase-1 (SCD-1) converting saturated lipids into MUPCs, which is thought to play an important role in cancer progression.[59] Compared with the corresponding H&E-stained sections, the tumor cells region is clearly observed in the MS imaging. Therefore, the accuracy of the histopathological diagnosis of tumors could be improved by mapping the distribution of multiple biomarkers. This result emphasizes that MS images of lipid biomarkers discovered *via* tissue imprinting TCSI-MSI could clearly delineate the tumor and normal tissue, showing an extraordinary superiority for the discrinmination of tumor tissues. While the obtained results revealed the diagnostic potential of TCSI-MSI, further studies are necessary to validate the results with a larger sample cohort to provide a more robust diagnosis model.

CONCLUSIONS

In summary, we have developed a TCSI-MSI platform based on 2D nanoflakes-capped SiNWs as a tissue imprinting substrate for lipidomic imaging and cancer diagnosis. Using NGQD as both an intercalation agent and dispersant, stable and few-layered 2D MoS_2 nanoflakes were obtained by forming NGQD@MoS_2 composites. The 2D NGQD@MoS_2 nanoflakes could be homogeneously loaded on the top of vertical SiNWs *via* a simple self-assembly process to construct a 2D nanoflake-capped vertical nanowire structure. Owing to its good affinity for lipids and enhanced LDI ability benefitng from the interplay between different nanostructure, the NGQD@MoS_2/SiNWs could serve as a high-performance TCSI-MSI substrate for imprinting lipids from tissues and detect them without the need of a matrix spray as required for MALDI-MSI. In addition, the LDI efficiency on the whole surface of NGQD@MoS_2/SiNWs chip is more homogeneous, thereby eliminating the sweet-spots and displays a more uniform mass signal over the chip surface. These advantages guarantee the authentical mapping of molecular spatial distribution in a sliced tissue sample. As a proof of concept, we demonstrated the capability of the NGQD@MoS_2/SiNWs

https://doi.org/10.1021/acsnano.2c02616
ACS Nano 2022, 16, 6916−6928

substrate as an efficient TCSI-MSI platform for discovery, profiling, and imaging of lipid biomarkers distributed in NSCLC tissue. With the assistance of machine learning algorithm, precise discrimination of NSCLC tissues from the adjacent normal tissues was successfully achieved. We believe that the present work promises great potentials as a universal platform for precision diagnosis and drug discovery.

EXPERIMENTAL SECTION

Materials. Silicon wafers (p-type, thickness of 500 μm, resistivity of 5−10 Ω·cm) were purchased from Lijing Silicon Materials Co. (Quzhou, China). Hydrofluoric acid (HF, 40%) was purchased from Sinopharm Chemical Reagent Co. (Shanghai, China). Silver nitrate ($AgNO_3$), 3-aminopropyltriethoxysilane (APTES), 1-aminopyrene, and MoS_2 powder were purchased from Aladdin Co. (Shanghai, China). 1,2-Dipalmitoyl-*sn*-glycero-3-phosphoethanolamine (PE(32:0)), 1,2-distearoyl-*sn*-glycero-3-phosphocholine (PC(36:0)), 1,1′,1″-(1,2,3-propanetriyl) ester (TAG(48:0)), indigo, and thiabendazole analytical standards were purchased from Sigma-Aldrich Co. (Shanghai, China). Carboxymethyl cellulose (2.5%, CMC) was obtained from LEAGENE Co. All other reagents used in this experiment were of analytical grade and used without further purification.

Fabrication of NGQD@MoS_2/SiNWs Substrate. For the preparation of vertical SiNWs substrate, a metal-assited chemical etching (MACE) method was used to fabricate vertical SiNWs. In brief, a Si wafer (p-type, resistivity of 5−10 Ω·cm) was cleaned with O_2 plasma for 10 min and then etched in solution containing 4.8 M HF and 0.02 M $AgNO_3$ for 10 min (***CAUTION***: HF is highly toxic and volatile, which is harmful to the respiratory system and skeleton. Contact of HF with skin should be avoided, and all the etching experiments need to be handled carefully in the fume hood). After etching, the wafers were washed repeatedly with water and then were immersed in dilute HNO_3 (HNO_3/DI water = 1:1) for 1 h to dissolve the Ag catalyst followed by a thorough wash with ultrapure water.

The preparation method of NGQD has been previously reported.[42] 1-Aminopyrene (2 mg/mL) was added to 200 mL of ammonia (0.4 M). The mixture was added to the torrefaction reactor, followed by a reaction of 8 h under 200 °C of temperature and high pressure. Afterward, the prepared solution was filtered through a 0.22 μm cellulose filter to remove particles with a large diameter. Then, adequate dialysis was conducted (cutoff >3500 Da, < 500 Da) to remove small molecules. After freeze-drying of the obtained solution, NGQD solid dispersion was prepared.

NGQD@MoS_2 nanoflake was synthesized by NGQD-assisted liquid phase exfoliation of MoS_2 powder. The MoS_2 powders were dispersed in 50% EtOH with a concentration of 7.5 mg/mL. In the meantime, a slight excess of NGQD suspension (1 mg/mL) was added to be 3.75% of the final volume. The dispersions were sonicated by using a point probe (flathead sonic tip) for 120 min with a power output of 250 W (JY88-IIN, SCIENTZ, Ningbo, China), followed by centrifugation at 7000 rpm for 20 min to remove unexfoliated MoS_2. After centrifugation, the top two-thirds of the dispersions was removed by gently pipetting into a separate tube. The supernatant was collected and centrifuged at 14 000 rpm to separate the exfoliated NGQD@MoS_2 nanoflakes. The NGQD@MoS_2 nanoflakes were washed with water three times and then dispersed in water.

To improve NGQD@MoS_2 nanoflake adhesion, the surface of SiNWs substrates was premodified with 4% APTES in toluene solution for 20 min, sonicated in toluene for 2 min, washed with ethanol, and dried under a stream of nitrogen. Afterward, the modified SiNWs substrates were immersed in 0.5 mg/mL NGQD@MoS_2 nanoflakes suspension for 5−60 min and subsequently rinsed by DI water. These NGQD@MoS_2/SiNWs chips were washed with water and ethanol and dried under a stream of nitrogen before use.

Characterization. The morphology of NGQD@MoS_2 nanoflakes was observed by transmission electron microscopy (TEM, H-7650, Hitachi Co., Tokyo, Japan). The size and morphology of NGQD@MoS_2 nanoflakes were obtained with an AFM (Park Systems, NX10, Suwon, Korea). The hydrodynamic diameter and ζ potential of NGQD@MoS_2 nanoflakes were measured by dynamic light scattering (DLS, ZEN 3600, MALVERN, Worcestershire, UK). The morphology of NGQD@MoS_2/SiNWs substrate was characterized by a scanning electron microscope (SEM, SU8010, Hitachi Co., Tokyo, Japan). X-ray photoelectron spectroscopy (XPS) spectra were obtained using Escalab 250Xi, Thermo. The UV−vis DRS spectra were recorded on a Shimadzu UV-3150 UV−vis spectrophotometer (Shimadzu, Kyoto, Japan). The absorbance spectra of NGQD@MoS_2 and MoS_2 nanoflakes in 7 days were measured to test the water stability with a SP-756PC UV−vis spectrometer (Shanghai Spectrum, Shanghai, China). The stability of NGQD@MoS_2 and MoS_2 was calculated according to the following formula:

stability (%) = $A/A_0 \times 100$, where A and A_0 represent absorbance at 670 nm of the suspension at test day and 0 day, respectively.

Sample Preparation. For lipids standard solutions, 1 mg/mL was prepared by diluting each solid lipid in CH_3Cl. Indigo (1 mg/mL) and 0.1 mM BP standard solution were, respectively, dissolved in a mixture of MeOH and H_2O (v/v = 1:1).

Nude mice (male, 6−8 week years old) for lung tissue imaging were purchased from Slack Corp. (Shanghai, China). Animal studies were performed in accordance with the guidelines of the Laboratory Animal Center of Zhejiang University, and the animal experimental protocols were approved by the Laboratory Animal Center of Zhejiang University. Clinical NSCLC tissue samples, including tumor and adjacent normal tissues, were obtained from NSCLC patients who underwent surgery at Sir Run Run Shaw Hospital. Informed consent was obtained from each patient and monitored by the Sir Run Run Shaw Hospital Ethics Review Board (Ethical review No. 20210322-32). Fresh frozen tissues were stored at −80 °C in a freezer before use. Carboxymethyl cellulose (CMC) 2.5% solution was used for tissue embedding prior to the frozen sectioning on a microtome cryostat. A 10 μm frozen section of each frozen tissue core sample was stained with hematoxylin and eosin (H&E), and then, a 50 μm section was obtained immediately adjacent to the H&E section using a CryoStar NX50 cryostat (Thermo Fisher Scientific) for imprinting LDI-MSI analysis.

LDI-MS Analysis. Droplets of 1.5 μL were spotted in three replicates onto substrates before detection. Mass spectra were obtained on an UltrafleXtreme MALDI-TOF/TOF-MS instrument (Bruker Daltonics Co.) equipped with a 355 nm Nd:YAG laser beam (pulse energy <500 μJ with a pulse width = 3 ns). The ions that resulted from a 100 ns pulse ion extraction were subjected to an electric field of 2.25 kV between ion source 1 and ion source 2 and were analyzed in reflective mode. The generated spectra were obtained after 2000 laser shots of the spot.

Tissue Imprinting-Based TCSI-MSI Analysis. A 50 μm tissue section was transferred onto a precooled substrate, and then, the underside of the substrate was carefully pressed on the back of a hand. After the warm substrate and tissue section were sufficiently warm, the imprinting process lasted for 1 min. Immediately after, the tissue section was removed with distilled water. The substrate was placed under room temperature until fully dried before conducting mass spectrometry imaging. MSI data were acquired using an UltrafleXtreme MALDI-TOF/TOF-MS instrument (Bruker Daltonics Co.) equipped with a 355 nm Nd:YAG laser beam. The basic instrument settings are same as the LDI-MS analysis. MSI acquisitions of lung tissues were carried out in positive ion reflective mode in 400−1000 Da mass range, with a lateral resolution of 150 μm. The laser shots were 500 s per pixel, and the spot size was 25 μm in diameter.

Statistical Analysis. The raw MS data was analyzed by FlexAnalysis software (Bruker Daltonics Co.). The raw MSI image data was visualized using FlexImaging software (Bruker Daltonics Co.), and the overall averaged spectra was exported. The mass ion images were visualized and processed by MSiReader v1.02 (a free, open source MATLAB user interface designed to read and process MSI data). Intensity was normalized by total ion count (TIC), and mass error tolerance was set to 50 ppm.

https://doi.org/10.1021/acsnano.2c02616
ACS Nano 2022, 16, 6916−6928

For construct a prediction model, the molecular peaks with $S/N > 5$ were selected from acquired overall averaged mass spectra. After isotope peaks exclusion, a total of 45 molecules were selected, and their intensities were normalized by TIC. Orthogonal partial least-squares discrimination analysis (OPLS-DA) of all NSCLC tissues and the adjacent normal tissues data were both conducted in SIMCA software (Umet rics, Umea, Sweden) for features screening. Two-sample two-sided Student's t test (95% CI) was also completed through the "ttest2" function in MATLAB software. Molecules that meet the condition of VIP > 1 in OPLS-DA and $p < 10^{-4}$ in t test were selected out, indicating a significant difference between tumor and normal samples. To visualize the degree of discrimination, hierarchical clustering analysis was performed on the basis od the selected features by R 3.5.2 software. Also, an artificial neural network (ANN) model with a multilayer perception structure (number of hidden neurons = 10) was built in the pattern recognition tool in MATLAB software on the basis of the feature peaks data set. In the ANN model, data from 48 tissues were for the modeling group and 12 tissues were for the test group. The detailed workflow is presented in Figure S10.

MS/MS experiments on MALDI-TOF/TOF MS were conducted to identify lipids structures corresponding to feature MS peaks. Through the LIPID MAPS database, the obtained fragmentation information can be aligned.

ASSOCIATED CONTENT

Supporting Information

The Supporting Information is available free of charge at https://pubs.acs.org/doi/10.1021/acsnano.2c02616.

Figures of fabrication and characterization of SiNWs, characterization of NGQDs, characterization of MoS_2 nanosheets, hydrodynamic radius spectrum and stability determination of NGQD@MoS_2 nanoflakes, ζ potential distribution of NGQD@MoS_2 nanoflakes, XPS spectrum of NGQD@MoS_2/SiNWs, uniformity of signal intensity distributed on the substrate, raw mass spectra of model molecule and comparison of total ion intensity on different substrates, workflow of artificial neural network (ANN) and calculation results and tables of patient information for NSCLC samples, potential biomarkers of NSCLC, and putative identification of biomarkers (PDF)

AUTHOR INFORMATION

Corresponding Authors

Fengna Xi − *Department of Chemistry, Key Laboratory of Surface & Interface Science of Polymer Materials of Zhejiang Province, Zhejiang Sci-Tech University, Hangzhou 310018, P. R. China;* orcid.org/0000-0001-8564-8911; Phone: 86-137-5826-0408; Email: fengnaxi@zstu.edu.cn

Zhengfu He − *Department of Thoracic Surgery, Sir Run Run Shaw Hospital, School of Medicine, Zhejiang University, Hangzhou 310016, P. R. China;* orcid.org/0000-0003-3167-9493; Phone: 86-138-6712-0566; Email: hezhengfu123@hotmail.com

Jianmin Wu − *Lab of Nanomedicine and Omic-based Diagnostics, Institute of Analytical Chemistry, Department of Chemistry, Zhejiang University, Hangzhou 310058, P. R. China;* orcid.org/0000-0002-0999-9194; Phone: 86-139-5813-5820; Email: wjm-st1@zju.edu.cn

Authors

Xingyue Liu − *Lab of Nanomedicine and Omic-based Diagnostics, Institute of Analytical Chemistry, Department of Chemistry, Zhejiang University, Hangzhou 310058, P. R. China*

Zhao Chen − *Department of Thoracic Surgery, Sir Run Run Shaw Hospital, School of Medicine, Zhejiang University, Hangzhou 310016, P. R. China*

Tao Wang − *Lab of Nanomedicine and Omic-based Diagnostics, Institute of Analytical Chemistry, Department of Chemistry, Zhejiang University, Hangzhou 310058, P. R. China*

Xinrong Jiang − *Lab of Nanomedicine and Omic-based Diagnostics, Institute of Analytical Chemistry, Department of Chemistry, Zhejiang University, Hangzhou 310058, P. R. China*

Xuetong Qu − *Lab of Nanomedicine and Omic-based Diagnostics, Institute of Analytical Chemistry, Department of Chemistry, Zhejiang University, Hangzhou 310058, P. R. China*

Wei Duan − *Lab of Nanomedicine and Omic-based Diagnostics, Institute of Analytical Chemistry, Department of Chemistry, Zhejiang University, Hangzhou 310058, P. R. China;* orcid.org/0000-0002-6609-1043

Complete contact information is available at: https://pubs.acs.org/10.1021/acsnano.2c02616

Author Contributions

‖X.L. and Z.C. contributed equally to this work. J.W. conceived the project and supervised the research. Z.H. provided the clinical sample and designed the clinical test. F.X. proposed the idea of material prepration. X.L. and Z.C. designed and performed the experiments. X.L., T.W., X.Q., X.J., and W.D. discussed the data and checked the manuscript. X.L. and J.W. wrote the paper. All authors have given approval to the final version of the manuscript.

Notes

The authors declare no competing financial interest.

ACKNOWLEDGMENTS

The authors acknowledge the financial support from the National Natural Science Foundation of China (No. 21575127, No. 21874118) and Well-healthcare Technologies Co., LTD.

REFERENCES

(1) Ferreri, C.; Sansone, A.; Ferreri, R.; Amézaga, J.; Tueros, I. Fatty Acids and Membrane Lipidomics in Oncology: A Cross-Road of Nutritional, Signaling and Metabolic Pathways. *Metabolites* **2020**, *10* (9), 345.

(2) Sullivan, L. B.; Gui, D. Y.; Heiden, M. G. V. Altered Metabolite Levels in Cancer: Implications for Tumour Biology and Cancer Therapy. *Nat. Rev. Cancer* **2016**, *16* (11), 680−693.

(3) Zhu, Z.; Zhang, L.; Lv, J.; Liu, X.; Wang, X. Trans-Omic Profiling Between Clinical Phenoms and Lipidomes Among Patients with Different Subtypes of Lung Cancer. *Clin. Transl. Med.* **2020**, *10* (4), e150−e151.

(4) Zhang, L.; Zhu, B.; Zeng, Y.; Shen, H.; Zhang, J.; Wang, X. Clinical Lipidomics in Understanding of Lung Cancer: Opportunity and Challenge. *Cancer Lett.* **2020**, *470*, 75−83.

(5) Matsushita, Y.; Nakagawa, H.; Koike, K. Lipid Metabolism in Oncology: Why It Matters, How to Research, and How to Treat. *Cancers* **2021**, *13* (3), 474.

(6) Buck, A.; Aichler, M.; Huber, K.; Walch, A. *Applications of Mass Spectrometry Imaging to Cancer*; Elsevier: Amsterdam, 2017; Vol. *134*, pp 117−132.

(7) Kriegsmann, J.; Kriegsmann, M.; Casadonte, R. MALDI TOF Imaging Mass Spectrometry in Clinical Pathology: A Valuable Tool for Cancer Diagnostics (Review). *Int. J. Oncol.* **2015**, *46* (3), 893−906.
(8) Müller, W. H.; De Pauw, E.; Far, J.; Malherbe, C.; Eppe, G. Imaging Lipids in Biological Samples with Surface-assisted Laser Desorption/Ionization Mass Spectrometry: A Concise Review of The Last Decade. *Prog. Lipid Res.* **2021**, *83*, 101114.
(9) Calvano, C. D.; Monopoli, A.; Cataldi, T. R.; Palmisano, F. MALDI Matrices for Low Molecular Weight Compounds: An Endless Story? *Anal. Bioanal. Chem.* **2018**, *410* (17), 4015−4038.
(10) Phan, N. T. N.; Mohammadi, A. S.; Dowlatshahi Pour, M.; Ewing, A. G. Laser Desorption Ionization Mass Spectrometry Imaging of Drosophila Brain Using Matrix Sublimation versus Modification with Nanoparticles. *Anal. Chem.* **2016**, *88* (3), 1734−1741.
(11) Samarah, L. Z.; Vertes, A. Mass Spectrometry Imaging Based on Laser Desorption Ionization from Inorganic and Nanophotonic Platforms. *View* **2020**, *1* (4), 20200063.
(12) Chen, W. T.; Tomalová, I.; Preisler, J.; Chang, H. T. Analysis of Biomolecules through Surface-Assisted Laser, Desorption/Ionization Mass Spectrometry Employing Nanomaterials. *J. Chin. Chem. Soc.* **2011**, *58* (6), 769−778.
(13) Law, K. P.; Larkin, J. R. Recent Advances in SALDI-MS Techniques and Their Chemical and Boanalytical Applications. *Anal. Bioanal. Chem.* **2011**, *399* (8), 2597−2622.
(14) Cha, S.; Yeung, E. S. Colloidal Graphite-Assisted Laser Desorption/Ionization Mass Spectrometry and MSn of Small Molecules. 1. Imaging of Cerebrosides Directly from Rat Brain Tissue. *Anal. Chem.* **2007**, *79* (6), 2373−2385.
(15) Xu, Y.; Deng, Y.; Ye, R.; Gong, C.; Liu, Z.; Zhao, Y.; Lu, Y.; Liu, J.; Xu, X. MALDI-MS Imaging of Lipids and Small Molecules in Rat Brain Tissue Based on Graphene Oxide Film Pre-Coated Matrix. *Int. J. Mass Spectrom.* **2021**, *464*, 116573.
(16) Kim, Y.-K.; Na, H.-K.; Kwack, S.-J.; Ryoo, S.-R.; Lee, Y.; Hong, S.; Hong, S.; Jeong, Y.; Min, D.-H. Synergistic Effect of Graphene Oxide/MWCNT Films in Laser Desorption/Ionization Mass Spectrometry of Small Molecules and Tissue Imaging. *ACS Nano* **2011**, *5* (6), 4550−4561.
(17) Nizioł, J.; Ossoliński, K.; Ossoliński, T.; Ossolińska, A.; Bonifay, V.; Sekuła, J.; Dobrowolski, Z.; Sunner, J.; Beech, I.; Ruman, T. Surface-Transfer Mass Spectrometry Imaging of Renal Tissue on Gold Nanoparticle Enhanced Target. *Anal. Chem.* **2016**, *88* (14), 7365−7371.
(18) Wang, X.-N.; Li, B. Monolithic Gold Nanoparticles/Thiol-β-cyclodextrin-Functionalized TiO2 Nanowires for Enhanced SALDI MS Detection and Imaging of Natural Products. *Anal. Chem.* **2022**, *94* (2), 952−959.
(19) Sun, R.; Tang, W.; Li, B. Gold-TiO_2@Gallic Acid Nanospheres for Enhanced Surface-Assisted Laser Desorption/Ionization Mass Spectrometry Imaging. *Appl. Mater. Today* **2022**, *26*, 101336.
(20) Ozawa, T.; Osaka, I.; Hamada, S.; Murakami, T.; Miyazato, A.; Kawasaki, H.; Arakawa, R. Direct Imaging Mass Spectrometry of Plant Leaves Using Surface-assisted Laser Desorption/Ionization with Sputter-deposited Platinum Film. *Anal. Sci.* **2016**, *32* (5), 587−591.
(21) Wei, J.; Buriak, J. M.; Siuzdak, G. Desorption−Ionization Mass Spectrometry on Porous Silicon. *Nature* **1999**, *399* (6733), 243−246.
(22) Fincher, J. A.; Dyer, J. E.; Korte, A. R.; Yadavilli, S.; Morris, N. J.; Vertes, A. Matrix-free Mass Spectrometry Imaging of Mouse Brain Tissue Sections on Silicon Nanopost Arrays. *J. Comp. Neurol.* **2019**, *527* (13), 2101−2121.
(23) Dufresne, M.; Fincher, J. A.; Patterson, N. H.; Schey, K. L.; Norris, J. L.; Caprioli, R. M.; Spraggins, J. M. α-Cyano-4-hydroxycinnamic Acid and Tri-Potassium Citrate Salt Pre-Coated Silicon Nanopost Array Provides Enhanced Lipid Detection for High Spatial Resolution MALDI Imaging Mass Spectrometry. *Anal. Chem.* **2021**, *93* (36), 12243−12249.
(24) Chen, X.; Wang, T.; Lin, L.; Wo, F.; Liu, Y.; Liang, X.; Ye, H.; Wu, J. Tip-Enhanced Photoinduced Electron Transfer and Ionization on Vertical Silicon Nanowires. *ACS Appl. Mater. Interfaces* **2018**, *10* (17), 14389−14398.
(25) Chen, X.; Gao, J.; Wang, T.; Jiang, X.; Chen, J.; Liang, X.; Wu, J. Hepatocarcinoma Discrimination by Ratiometric Lipid Profiles Using Tip-Contact Sampling/Ionization Mass Spectrometry. *Anal. Chem.* **2019**, *91* (16), 10376−10380.
(26) Iakab, S. A.; Ràfols, P.; Tajes, M.; Correig-Blanchar, X.; García-Altares, M. Gold Nanoparticle-Assisted Black Silicon Substrates for Mass Spectrometry Imaging Applications. *ACS Nano* **2020**, *14* (6), 6785−6794.
(27) Rudd, D. A.; Benkendorff, K.; Chahal, C.; Guinan, T.; Gustafsson, O. J. R.; Esmaeelian, B.; Krysinska, H.; Pogson, L.; Voelcker, N. H.; Abbott, C. A. Mapping Insoluble Indole Metabolites in The Gastrointestinal Environment of A Murine Colorectal Cancer Model Using Desorption/Ionisation on Porous Silicon Imaging. *Sci. Rep.* **2019**, *9* (1), 1−13.
(28) Xu, Q.; Tian, R.; Lu, C.; Li, H. Monodispersed Ag Nanoparticle in Layered Double Hydroxides as Matrix for Laser Desorption/Ionization Mass Spectrometry. *ACS Appl. Mater. Interfaces* **2018**, *10* (51), 44751−44759.
(29) Zhao, Y.; Liao, Q.; Xi, K.; Xu, D. MoS_2-Assisted LDI Mass Spectrometry for the Detection of Small Molecules and Quantitative Analysis of Sulfonamides in Serum. *J. Am. Soc. Mass Spectrome* **2021**, *32* (9), 2463−2471.
(30) Chu, H.-W.; Unnikrishnan, B.; Anand, A.; Mao, J.-Y.; Huang, C.-C. Nanoparticle-based Laser Desorption/Ionization Mass Spectrometric Analysis of Drugs and Metabolites. *J. Food. Drug. Anal* **2018**, *26* (4), 1215−1228.
(31) Xue, J.; Liu, H.; Chen, S.; Xiong, C.; Zhan, L.; Sun, J.; Nie, Z. Mass Spectrometry Imaging of the In Situ Drug Release From Nanocarriers. *Sci. Adv.* **2018**, *4* (10), No. eaat9039.
(32) Kim, Y.-K.; Wang, L.-S.; Landis, R.; Kim, C. S.; Vachet, R. W.; Rotello, V. M. A Layer-by-Layer Sssembled MoS_2 Thin Film as an Efficient Platform for Laser Desorption/Ionization Mass Spectrometry Analysis of Small Molecules. *Nanoscale* **2017**, *9* (30), 10854−10860.
(33) Wu, R.; Ou, X.; Tian, R.; Zhang, J.; Jin, H.; Dong, M.; Li, J.; Liu, L. Membrane Destruction and Phospholipid Extraction by Using Two-Dimensional MoS_2 Nanosheets. *Nanoscale* **2018**, *10* (43), 20162−20170.
(34) Jiang, D.; Du, X.; Zhou, L.; Li, H.; Wang, K. New Insights Toward Efficient Charge-Separation Mechanism for High-Performance Photoelectrochemical Aptasensing: Enhanced Charge-Carrier Lifetime *via* Coupling Ultrathin MoS_2 Nanoplates with Nitrogen-doped Graphene Quantum Dots. *Anal. Chem.* **2017**, *89* (8), 4525−4531.
(35) Li, S.; Ma, W.; Zhou, Y.; Chen, X.; Xiao, Y.; Ma, M.; Wei, F.; Yang, X. Fabrication of P-Type Porous Silicon Nanowire with Oxidized Silicon Substrate Through One-Step MACE. *J. Solid State Chem.* **2014**, *213*, 242−249.
(36) Gong, J.; Zhang, Z.; Zeng, Z.; Wang, W.; Kong, L.; Liu, J.; Chen, P. Graphene Quantum Dots Assisted Exfoliation of Atomically-Thin 2D Materials and As-Formed 0D/2D Van Der Waals Heterojunction for HER. *Carbon* **2021**, *184*, 554−561.
(37) Min, M.; Sakri, S.; Saenz, G. A.; Kaul, A. B. Photophysical Dynamics in Semiconducting Graphene Quantum Dots Integrated with 2D MoS_2 for Optical Enhancement in the Near UV. *ACS Appl. Mater. Interfaces* **2021**, *13* (4), 5379−5389.
(38) Jiang, D.; Liu, Z.; Xiao, Z.; Qian, Z.; Sun, Y.; Zeng, Z.; Wang, R. Flexible Electronics Based on 2D Transition Metal Dichalcogenides. *J. Mater. Chem. A* **2021**, *10* (1), 89−121.
(39) Qiao, L.; Liao, M.; Fang, K.; He, X.; Zhang, Y. Enhancement of Photoelectrochemical Hydrogen Evolution of P-Type Silicon Nanowires Array by Loading MoS_2. *Silicon* **2019**, *11* (4), 1963−1970.
(40) Alarawi, A.; Ramalingam, V.; Fu, H.-C.; Varadhan, P.; Yang, R.; He, J.-H. Enhanced Photoelectrochemical Hydrogen Production Efficiency of MoS_2-Si heterojunction. *Opt. Express* **2019**, *27* (8), A352−A363.

https://doi.org/10.1021/acsnano.2c02616
ACS Nano 2022, 16, 6916−6928

(41) Che, H.; Liu, C.; Hu, W.; Hu, H.; Li, J.; Dou, J.; Shi, W.; Li, C.; Dong, H. NGQD active sites as Effective Collectors of Charge Carriers for Improving the Photocatalytic Performance of Z-Scheme gC_3N_4/Bi_2WO_6 Heterojunctions. *Catal. Sci. Technol.* **2018**, *8* (2), 622−631.
(42) Wan, Y.; Zhao, J.; Deng, X.; Chen, J.; Xi, F.; Wang, X. Colorimetric and Fluorescent Dual-Modality Sensing Platform Based on Fluorescent Nanozyme. *Front. Chem.* **2021**, *9* (995), 774486.
(43) Xue, Y.; Maduraiveeran, G.; Wang, M.; Zheng, S.; Zhang, Y.; Jin, W. Hierarchical Oxygen-Implanted MoS_2 Nanoparticle Decorated Graphene for the Non-Enzymatic Electrochemical Sensing of Hydrogen Peroxide in Alkaline Media. *Talanta* **2018**, *176*, 397−405.
(44) Hamdi, A.; Boussekey, L.; Roussel, P.; Addad, A.; Ezzaouia, H.; Boukherroub, R.; Coffinier, Y. Hydrothermal Preparation of MoS_2/TiO_2/Si Nanowires Composite with Enhanced Photocatalytic Performance Under Visible Light. *Mater. De.* **2016**, *109*, 634−643.
(45) Chatterjee, M.; Mondal, P.; Beyer, K.; Paretzki, A.; Kaim, W.; Lahiri, G. K. A Structurally Characterised Redox Pair Involving an Indigo Radical: Indigo Based Redox Activity in Complexes With One or Two [Ru (bpy) 2] Fragments. *Dalton Trans* **2017**, *46* (15), 5091−5102.
(46) Yin, Y.; Liu, Q.; Jiang, D.; Du, X.; Qian, J.; Mao, H.; Wang, K. Atmospheric Pressure Synthesis of Nitrogen Doped Graphene Quantum Dots for Fabrication of BiOBr Nanohybrids with Enhanced Visible-Light Photoactivity and Photostability. *Carbon* **2016**, *96*, 1157−1165.
(47) Song, K.; Cheng, Q. Desorption and Ionization Mechanisms and Signal Enhancement in Surface Assisted Laser Desorption Ionization Mass Spectrometry (SALDI-MS). *Appl. Spectrosc. Rev.* **2020**, *55* (3), 220−242.
(48) Tang, L. A. L.; Wang, J.; Loh, K. P. Graphene-Based SELDI Probe with Ultrahigh Extraction and Sensitivity for DNA Oligomer. *J. Am. Chem. Soc.* **2010**, *132* (32), 10976−10977.
(49) Müller, W. H.; Verdin, A.; De Pauw, E.; Malherbe, C.; Eppe, G. Surface-Assisted Laser Desorption/Ionization Mass Spectrometry Imaging: A Review. *Mass Spectrom. Rev.* **2022**, *41* (3), 373.
(50) Nguyen, S. N.; Kyle, J. E.; Dautel, S. E.; Sontag, R.; Luders, T.; Corley, R.; Ansong, C.; Carson, J.; Laskin, J. Lipid Coverage in Nanospray Desorption Electrospray Ionization Mass Spectrometry Imaging of Mouse Lung Tissues. *Anal. Chem.* **2019**, *91* (18), 11629−11635.
(51) Tata, A.; Fernandes, A. M. A. P.; Santos, V. G.; Alberici, R. M.; Araldi, D.; Parada, C. A.; Braguini, W.; Veronez, L.; Silva Bisson, G.; Reis, F. H. Z.; Alberici, L. C.; Eberlin, M. N. Nanoassisted Laser Desorption-Ionization-MS Imaging of Tumors. *Anal. Chem.* **2012**, *84* (15), 6341−6345.
(52) Moening, T. N.; Brown, V. L.; He, L. Matrix-enhanced Nanostructure Initiator Mass Spectrometry (ME-NIMS) for Small Molecule Detection and Imaging. *Anal. Methods* **2016**, *8* (46), 8234−8240.
(53) Jackson, S. N.; Baldwin, K.; Muller, L.; Womack, V. M.; Schultz, J. A.; Balaban, C.; Woods, A. S. Imaging of Lipids in Rat Heart by MALDI-MS with Silver Nanoparticles. *Anal. Bioanal. Chem.* **2014**, *406* (5), 1377−1386.
(54) Bray, F.; Ferlay, J.; Soerjomataram, I.; Siegel, R. L.; Torre, L. A.; Jemal, A. Global Cancer Satistics 2018: GLOBOCAN Estimates of Incidence and Mortality Worldwide for 36 Cancers in 185 Countries. *CA: Cancer J. Clin.* **2018**, *68* (6), 394−424.
(55) Fessler, M. B.; Summer, R. S. Surfactant Lipids at The Host−Environment Interface. Metabolic Sensors, Suppressors, and Effectors of Inflammatory Lung Disease. *Am. J. Respir. Cell Mol. Biol.* **2016**, *54* (5), 624−635.
(56) Li, T.; He, J.; Mao, X.; Bi, Y.; Luo, Z.; Guo, C.; Tang, F.; Xu, X.; Wang, X.; Wang, M.; Chen, J.; Abliz, Z. In Situ Biomarker Discovery and Label-free Molecular Histopathological Diagnosis of Lung Cancer by Ambient Mass Spectrometry Imaging. *Sci. Rep.* **2015**, *5* (1), 14089.
(57) Marien, E.; Meister, M.; Muley, T.; Fieuws, S.; Bordel, S.; Derua, R.; Spraggins, J.; Van de Plas, R.; Dehairs, J.; Wouters, J.; et al. Non-Small Cell Lung Cancer is Characterized by Dramatic Changes in Phospholipid Profiles. *Int. J. Cancer* **2015**, *137* (7), 1539−1548.
(58) Muranishi, Y.; Sato, T.; Ito, S.; Satoh, J.; Yoshizawa, A.; Tamari, S.; Ueda, Y.; Yutaka, Y.; Menju, T.; Nakamura, T.; Date, H. The Ratios of Monounsaturated to Saturated Phosphatidylcholines in Lung Adenocarcinoma Microenvironment Analyzed by Liquid Chromatography-Mass Spectrometry and Imaging Mass spectrometry. *Sci. Rep.* **2019**, *9* (1), 8916.
(59) Noto, A.; Raffa, S.; De Vitis, C.; Roscilli, G.; Malpicci, D.; Coluccia, P.; Di Napoli, A.; Ricci, A.; Giovagnoli, M.; Aurisicchio, L.; et al. Stearoyl-CoA Desaturase-1 is a Key Factor for Lung Cancer-Initiating Cells. *Cell Death Dis* **2013**, *4* (12), e947.

https://doi.org/10.1021/acsnano.2c02616
ACS Nano 2022, 16, 6916−6928